

Phase transition at 350 K in the $Ti_3C_2T_x$ MXene: possible sliding (moiré) ferroelectricity

Francesco Cordero,^{1,*} Hanna Pazniak,² Thierry Ouisse,² Jesus Gonzalez-Julian,³ Aldo Di Carlo,¹ Viktor Soprunyuk,⁴ and Wilfried Schranz⁴

¹*Istituto di Struttura della Materia-CNR (ISM-CNR), Area della Ricerca di Roma - Tor Vergata,
Via del Fosso del Cavaliere 100, I-00133 Roma, Italy*

²*Université Grenoble Alpes, CNRS, Grenoble INP, LMGP, 3 parvis Luviois Néel, F-38000 Grenoble, France*

³*Department of Ceramics, Institute of Mineral Engineering,*

RWTH Aachen University, D-52074 Aachen, Germany

⁴*Faculty of Physics, University of Vienna, Boltzmanngasse 5, 1090 Wien, Austria*

(Dated: October 25, 2023)

A phase transition is found in $Ti_3C_2T_x$ MXene at 350 K, by measuring the complex Young's modulus of self-standing thick films. A step-like softening and increase of the mechanical losses is found below 350 K, indicative of a phase transition, where the square of the order parameter is coupled to strain. It is argued that it should be a ferroelectric transition, most likely of the sliding (moiré) type, due to charge transfer between facing flakes sliding with respect to each other. If the transition will be confirmed to be ferroelectric, $Ti_3C_2T_x$ will be added to the class of metallic ferroelectrics and open new perspectives of applications, in addition to the numerous already studied.

Up to recent times it was believed that ferroelectric transitions cannot occur in materials with sizes below a certain limit. Indeed, the critical thickness for a film to sustain ferroelectricity (FE) is found to be of the order of tens of nanometers in ferroelectrics with perovskite or fluorite structure [1]. After the prediction of FE with giant piezoelectricity in the monolayer chalcogenides SnSe, SnS, GeSe, and GeS [2] and the experimental verifications that $CuInP_2S_6$ has a FE transition with $T_C = 320$ K [3, 4], the number of layered van der Waals (vdW) ferroelectrics has increased and includes α - In_2Se_3 [5], γ - $InSe$ [6], SnS [7], SnSe, SnTe [8], $1T'$ - $MoTe_2$ [9], $1T'$ - MoS_2 [10], and $1T'$ - WTe_2 [11, 12]. It has also been ascertained that in BN [13], MoS_2 [14] WTe_2 and few other systems a new mechanism, other than lattice instability, is responsible for FE, namely the relative sliding of the vdW stacked layers, called sliding or moiré FE [15–18] and can even be observed in multilayers of monoatomic graphene [19]. The phenomenon was first predicted for BN and mixed BN/graphene bilayers and other vdW bilayers [20] and is based on the charge transfer between the facing atoms in the two layers, which induces an out-of-plane polarization. The interest in these ferroelectric mono and bi-layers is great, in view of possible applications in nanoelectronics [17, 21], for example more miniaturized FeRAMs integrable with Si or other materials thanks to the vdW coupling. Especially the sliding or Moiré FE offers unique advantages of robust out-of-plane polarization [16].

MXenes are other 2D layered materials with chemical formula $M_{n+1}C_nT_x$ (M standing for a transition metal, X standing for C or N, and T_x is surface functional groups). In the MXene structure, the surface groups T_x (usually $-F$, $=O$, $-OH$), inherited from the etching environment, are covalently bound to the transition metal and weakly bound via van der Waals bonds to terminations of neighboring sheets. Such structures are being extensively studied for a multitude of possible applications in important sectors [22], such as electrodes

in Li/Na batteries [23], intermediate layers of perovskite solar cells [24], flexible and nano-electronics [25], soft robotics [26], catalysis and many others [22, 23]. However, no ferroelectricity has been found up to now in MXenes, but only theoretically predicted in Sc_2CO_2 [27]. On the other hand, $Ti_3C_2T_x$ monolayers have been demonstrated to be piezoelectric [28, 29]. Piezoelectricity, namely an induced strain proportional to an applied electric field or polarization induced by stress, is a consequence of FE, but is also possible in non-ferroelectrics lacking spontaneous polarization, if their lattice belongs to certain non-centrosymmetric classes. This is the case of bi-atomic hexagonal layers and of $Ti_3C_2T_x$ [28].

It must be said that the theoretical predictions of 2D FE are more numerous than the experimental verifications, which are rather challenging. In fact, these types of FE are probed on mono-, bi- or tri-layer nanoflakes with techniques such as Piezo-Force Microscopy (PFM) or conductive AFM.

We will show that these types of FE can be probed also with the simple macroscopic method of measuring the elastic anomaly associated with the FE transition on thick films of the layered material. We present the first measurements of the complex Young's modulus versus temperature of self-standing thick films of the $Ti_3C_2T_x$ MXene, which exhibit a clear and robust nearly second order phase transition at $\simeq 350$ K, and it is argued that, in spite of the good electrical conductivity, the transition should be ferroelectric, likely of the sliding type.

$Ti_3C_2T_x$ MXenes were synthesized by selective chemical etching of the Al layer from a parent Ti_3AlC_2 powder precursor using the minimally intensive layer delamination approach [30]. To produce a thick $Ti_3C_2T_x$ film, a suspension of well-delaminated flakes was vacuum filtered through a nitrocellulose membrane with an average pore size of $0.22 \mu m$. After drying, deposited layers were detached from the membrane, and a rigid thick free-standing MXene film was obtained. The film thickness was controlled by the concentration and the amount of filtered suspension.

The complex Young's modulus $E = E' + iE''$ was measured in an apparatus where a bar-shaped sample is suspended on

* francesco.cordero@ism.cnr.it

thin thermocouple wires in high vacuum ($< 10^{-5}$ mbar), and electrostatically excited on its free flexural resonant modes [31]. The resonance frequencies are $f \propto \sqrt{E}$ [32], so that the temperature dependence of E is evaluated as $E(T)/E_0 = [f(T)/f_0]^2$. The elastic energy loss coefficient, $Q^{-1} = E''/E'$, is measured from the decay of the free oscillations or the width of the resonance peak. The measurements are made well within the linear elastic limit. Details on some of the experimental difficulties encountered and their solutions can be found in the Supplemental Material (SM). The measurements reported here were made on a strip 25.5 mm long, 3 mm wide and (73 ± 4) μm thick, with the first three free flexural resonances clearly visible. In order to consolidate the film avoiding warping and bubbles (see SM), the sample was put between two alumina slabs and heated at 1.5 $^\circ\text{C}/\text{min}$ up to 700 $^\circ\text{C}$ in 10^{-6} mbar, kept 1 h and furnace cooled. The film became flat and more brittle. Thermal annealing has been reported to improve electrical conductivity of MXene films and we observed the same trend in the change in Young's modulus: after annealing it increased from 11.9 GPa to 44 GPa, presumably due to the loss of intercalated species.

The anelastic spectra were measured also using a Perkin-Elmer Diamond DMA in the three point bending mode, where flexural vibrations are forced at fixed frequencies in the range 0.1–10 Hz in Ar atmosphere (see SM). The sample were also characterized before and after the anelastic measurements by XRD, and Raman spectroscopy (see SM).

Figure 1 presents the Young's modulus E and elastic energy loss Q^{-1} measured during the 1st and 3rd cooling runs (empty symbols), and subsequent heating (filled symbols). In the last case, in addition to the fundamental also the 2nd and 3rd flexural modes were excited at higher frequencies. Until the sample was maintained in vacuum, the measurements were well repeatable, with some hysteresis between heating and cooling above room temperature. The main result is the nearly frequency independent negative step of E and positive step of Q^{-1} below $T_C \simeq 350$ K. The step in E is preceded by a precursor softening extending tens of kelvin above T_C . This is the typical signature of a phase transition whose squared order parameter is linearly coupled with strain [33, 34].

Above T_C the Young's modulus exhibits some frequency dispersion, that may be at least partly accounted for by the intense relaxation process labeled P2. In fact, this broad peak shifts to higher temperature with increase of frequency, indicating thermal activation of the spectrum of characteristic times and must be accompanied by a decrease of the real part, according to the Debye formula $\Delta E \propto (1 + i\omega\tau)^{-1}$ in the case of a single relaxation time τ ($\omega = 2\pi f$). There is also a minor peak in Q^{-1} , labeled P1, too small to produce visible effects on E .

These measurements have been repeated several times, to check their reproducibility also after exposure to air or immersion in water, as described in the SM. In brief, it was found that the anelastic spectrum was reproduced even when measured in 700 mbar water vapor up to 430 K, with little or no intercalation of H_2O . One day immersion in water resulted in intercalation of ~ 0.3 H_2O per formula unit, softening the modulus and strongly depressing the elastic anomaly

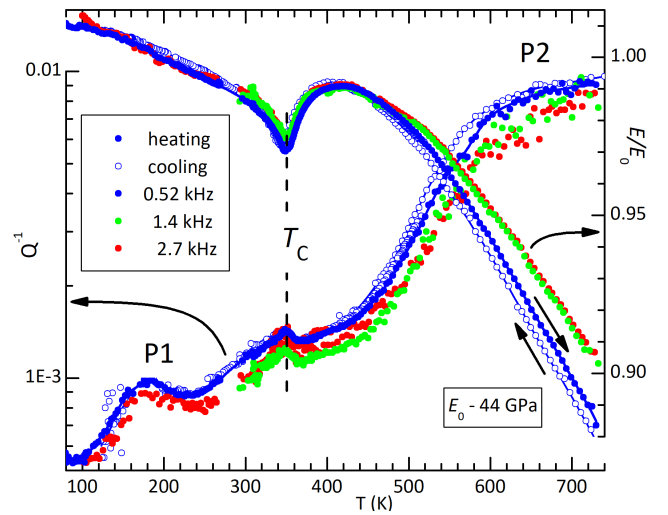


FIG. 1. Normalized Young's modulus and elastic energy loss measured during the 4th heating (filled symbols), exciting the 1st, 2nd and 3rd flexural modes. The empty symbols are the 1st and 3rd coolings.

at T_C . Outdiffusion of water in vacuum was fast above 430 K. The cycle of experiments was concluded with heating up to 890 K, after which the original Q^{-1} curve was completely recovered, but E remained $\sim 4\%$ softer and the step amplitude was smaller than originally (curve 12 in Figs. 2 and S1). This was probably also due to surface oxidation of the film, revealed by Raman spectroscopy after completing the anelastic measurements.

The DMA measurements substantially confirm all the previous ones with the resonance method, and provide additional information on the relatively slow dynamics characterizing the transition. A strip of as-prepared material had at room temperature a Young's modulus as low as 4 GPa, which increased up to 25 GPa after warming up to 495 K (not shown), confirming the consolidation effect of heating the as-deposited MXene sheet in vacuum or inert atmosphere. Figure 2 presents a DMA run from 200 to 810 K at 5 K/min and 0.1, 1, 10 Hz on the same sample that had been measured with the resonance method. Two months passed between the two sets of measurements. For comparison, the first and last runs with the resonance method are also shown, with the same labeling of Fig. S1. The major result is the confirmation of the steplike softening below 350 K. The magnitude of the modulus measured with the two methods is also in fair agreement, considering that the $E(T)$ curves are quite reproducible until the sample is measured and continuously kept in HV, but otherwise they can vary considerably.

The DMA measurements put in evidence a progressive stiffening of E with increase of frequency above T_C and a broad step around 700 K, that had appeared also in the last resonance heating (curve 11).

More interesting is the frequency dispersion at the phase transition, put in evidence in Fig. 3. The last heating with the resonance method (curve 11 of Fig. 2) is multiplied by 1.097

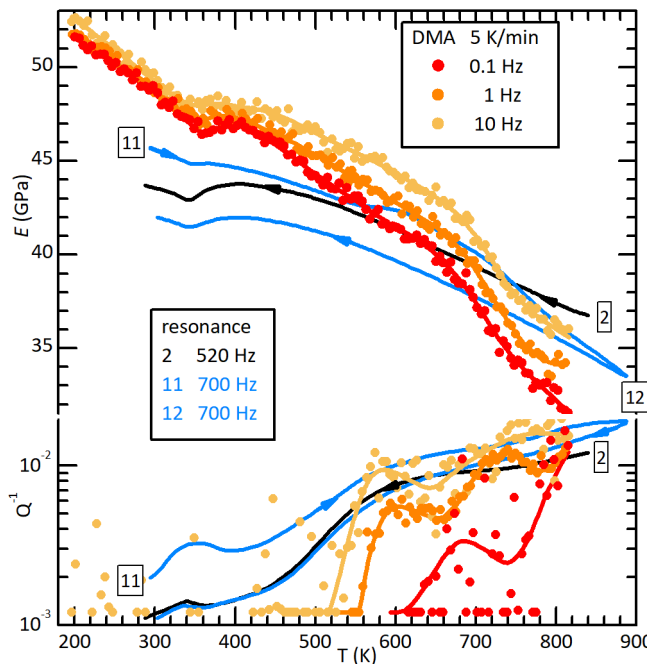


FIG. 2. Young's modulus and elastic energy loss measured with DMA at three frequencies heating at 5 K/min. The previous first and last runs with the resonance method are also shown, numbering the temperature scans in the same manner as in Fig. S1.

for clarity. A 10% difference in the magnitude of the Young's moduli measured with the two methods may be due to imperfect shape and homogeneity of the sample and is well within the 20% estimated absolute accuracy of the DMA method [35]. In addition, it may be partly due to the variability of the modulus following exposure to air and high temperature cycles.

XRD and Raman spectra were measured again after the above experiments, as described in the SM. The XRD spectra did not show any new peak, excluding decomposition and formation of new phases within the bulk of the film, but were shifted, indicating a decrease of the c lattice parameter from 26.35 to 20.22 Å. This is due to the loss of the initial intercalants. The Raman spectra, probing only the surface, exhibited new peaks attributable to TiO₂ (anatase), absent in the XRD spectrum, indicating that surface oxidation occurred.

The major result of these anelastic measurements is the presence of a previously unnoticed nearly second order phase transition at $T_C \simeq 350$ K.

The elastic anomaly consists of a negative step of $\sim 4\%$ in the Young's modulus E below T_C , accompanied by a positive step in the elastic energy loss Q^{-1} and preceded by precursor softening extending tens of kelvin above T_C . This type of anomaly is characteristic of a phase transition whose order parameter (OP) P is coupled with strain ϵ through a term $\propto \epsilon P^2$ in the free energy [33]. This is the case of a ferroelectric transition where P is the electric polarization, but also of a (anti)ferromagnetic or antiferrodistortive transition (like

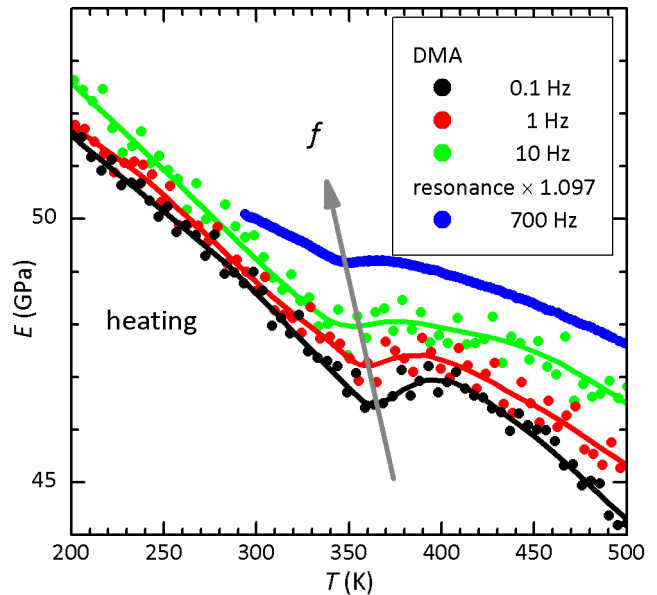


FIG. 3. Frequency dependence of the step in the Young's modulus at the phase transition. The resonance data are multiplied by 1.097.

octahedral tilting in perovskites [36]).

A magnetic transition can be excluded, since MXenes are mainly Pauli paramagnets. In some cases the magnetization of Ti₃C₂T_x is very small down to 60 K, where a small kink may indicate a paramagnetic-to-antiferromagnetic transition [37].

Regarding the possibility of an antiferrodistortive transition in vdW solids, we know of only two possibilities in layered organic-inorganic halide perovskites. One is coordinated Jahn-Teller distortions of the BX₆ octahedra [38], but this is not possible with Ti⁴⁺. The other is tilting of the octahedra [39]. This type of transition is common in perovskites AMX₃ [40], with short strong M-X bonds and longer weaker A-X bonds. When the network of rigid corner-sharing octahedra MX₆, sharing only their vertices X, cannot follow the thermal contraction of the more anharmonic A-X bonds, the rigid octahedra tilt in order to fit into the smaller lattice, giving rise to the antiferrodistortive transition. In Ti₃C₂T_x there are only Ti-C bonds, and the network of edge sharing CTi₆ octahedra [41] has neither the structural flexibility nor a driving force for an antiferrodistortive instability. Indeed, deviations from the in-plane hexagonal structure have never been reported, neither with traditional X-ray diffraction nor with its pair distribution function analysis [42].

Therefore, the remaining possibility is that the transition is ferroelectric. Indeed, the elastic anomaly in Ti₃C₂T_x is very similar to that found in classical ferroelectrics, for example in BaTiO_{3- δ} , observable both in the insulating state with $\delta = 0$ [43] and when the material is made metallic by introducing O vacancies [44]. The similarity is not limited to the steps in elastic modulus and damping, but includes a precursor softening extending at least tens of kelvin above T_C [43, 45]. The major difference between the elastic anomalies in Ti₃C₂T_x and BaTiO_{3- δ} is the magnitude of the softening, which is up

to 50% in BaTiO₃ and $\sim 4\%$ in Ti₃C₂T_x.

The ferroelectric nature of the transition, however, cannot be ascertained with the usual electric methods, since Ti₃C₂T_x is a good electric conductor and any applied electric field is shielded by the free charge carriers. There are only few known metallic ferroelectrics, among which is the vdW layered WTe₂ [12]. Probing FE in vdW layered materials is achieved through sophisticated experiments on mono-, bi- and tri-layer nanoflakes, but the task is particularly challenging in the case of electrically conducting materials. The present results show that the possible ferroelectric transition in Ti₃C₂T_x can be probed also with a macroscopic measurement like the temperature dependence of the complex elastic modulus of a self-standing thick film. Not only it is not necessary to probe the polarization switching at the atomic level, but the good electric conductivity of the sample, which hinders the transition to the usual electrical methods, does not affect the elastic properties, which therefore reveal the elastic anomaly from the coupling between strain and polarization.

As far as the elastic anomaly is concerned, FE in Ti₃C₂T_x may be due to the usual lowering of the symmetry of the paraelectric phase, like Ti off-centering in BaTiO₃ or vertical shifting of the intermediate Se plane in the vdW In₂Se₃ [46]. In the present case, a possibility would be vertical shifting of the C planes with respect to the Ti planes. This type of polar structure, however, has never been reported for Ti₃C₂T_x; rather, it has been found that monolayers are piezoelectric with null polarization in the absence of strain [28]. This corresponds to intrinsic piezoelectricity rather than switchable spontaneous polarization within a monolayer.

Ti₃C₂T_x presents similarities with bilayer WTe₂, which is both semi-metallic and ferroelectric with $T_C \simeq 350$ K [11, 15]. The origin of its FE has been identified with the relative sliding between layers, which forms out-of-plane electric dipoles, due to the transfer of electronic charge between the facing atoms. The fact that the electric dipoles are formed between pairs of layers and approximately perpendicular to them explains why the polarization is not completely screened by the in-plane conductivity [15]. Relative sliding of two facing monolayers can switch the polarization over an extended area without requiring atomic displacements within the monolayers. A clear indication that the transition is due to an interlayer mechanism, and not intrinsic of each layer, is the fact that it is not observed in the as-prepared state, abundantly intercalated, and disappears by intercalating water.

The Curie temperature in sliding FE is well above room temperature, even though the sliding barrier is of \lesssim meV [15]. This is very convenient for applications, since it combines low switching fields with robust ferroelectricity, and has been explained in the framework of continuum electromechanics as a consequence of the large in-plane rigidity of the layers [47]. For Ti₃C₂T_x there would be the complication that the facing species are not the ordered planes of surface Ti atoms but the -OH, =O and -F terminations. We are not aware of reports of sliding FE between non uniformly terminated layers, but will discuss the elastic anomaly in this light, though the analysis will be valid for any type of FE. In fact, we can exploit the fact that in semiconducting bilayer WSe₂, exhibiting sliding

FE, the spontaneous polarization $P(T)$ can be fitted with the usual Landau free energy with terms up to the 6th power of P [48],

$$F = \frac{a}{2}(T - T_C)P^2 + \frac{B}{4}P^4 + \frac{C}{6}P^6, \quad (1)$$

generally used for describing any first ($B < 0$) or second ($B > 0$) order ferroelectric transition. Once the transition is phenomenologically described in terms of Eq. (1), the elastic anomaly can be evaluated introducing a suitable coupling between stress/strain and order parameter P . We disregard a possible coupling of P with the "intrinsic" piezoelectricity found in the non-centrosymmetric monolayer of Ti₃C₂T_x [28], with in-plane polarization p , because p and P are approximately perpendicular to each other and physically separated. In fact, p is in-plane and confined by the good electrical conductivity within the layers, while P is approximately perpendicular to and between the layers. In addition, while p is due to the atomic displacements within the layers, P is considered to arise from interlayer electronic transfer with minimal relative atomic displacements within layers [17].

In order to evaluate the effect of the transition on the elastic modulus, we include in the free energy the elastic and the mixed terms containing both P and strain ε or, considering the Gibbs free energy $G = F - \sigma\varepsilon$, the terms containing P and stress σ . Without entering in the details of the mechanism causing the polarization, we can safely include the electrostrictive coupling $Q\sigma P^2$, always allowed [33, 49], while the piezoelectric coupling $d\sigma p$ is with the intrinsic p , so that

$$G = \frac{a}{2}(T - T_C)P^2 + \frac{B}{4}P^4 + \frac{C}{6}P^6 - \frac{S^0}{2}\sigma^2 - Q\sigma P^2 + (2) \\ + \frac{1}{2\chi_p}p^2 - d\sigma p, \quad (3)$$

where the susceptibility χ_p of p , nearly independent of T , is included.

The elastic compliance $S = 1/E$ is calculated as usual [33, 50, 51] as $S = d\varepsilon/d\sigma$ with $\varepsilon = -\partial G/\partial\sigma$ and one obtains (see SM)

$$S(T > T_C) = S^0 + \chi_p d^2 \\ S(T < T_C) = S^0 + \chi_p d^2 + \Delta S \\ \Delta S = \frac{2Q^2}{B\sqrt{\frac{T_C + \Delta T - T}{\Delta T}}}, \quad \Delta T = \frac{B^2}{4aC} \quad (4)$$

The constant term $\chi_p d^2$ is the softening due to the intrinsic piezoelectricity, and just reorganizes the background compliance S^0 . The coupling to P does not produce any effect in the paraelectric phase ($T > T_C$ for $B < 0$ and up to $T_C + \Delta T$ for $B < 0$), where P is null apart from fluctuations, and produces a steplike softening ΔS in the ferroelectric phase. The step is constant of magnitude $2Q^2/B$ if $C = 0$ and acquires a cusped shape for $C > 0$. This type of elastic anomaly is the same for any OP that is coupled quadratically to stress/strain, including magnetization and the rotation angle in antiferrodistortive transition, as in SrTiO₃ [36]. The softening is due to the relaxation of the order parameter upon application of stress, with

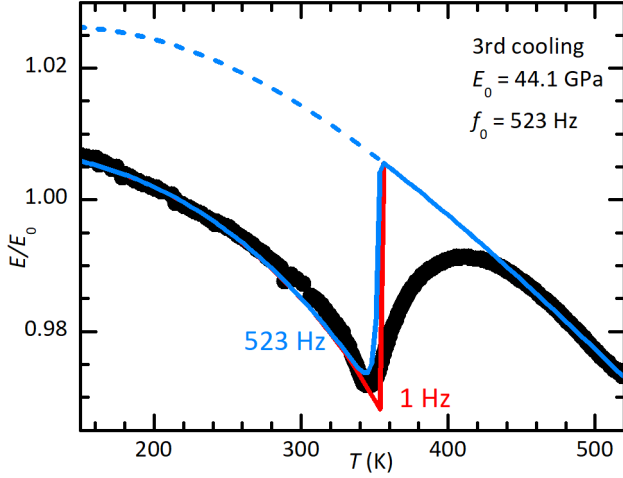


FIG. 4. Fit of the elastic anomaly presented in Fig. 1, measured at 523 Hz during the 3rd cooling, using Eq. (4) with the parameters $\Theta = 490$ K; $T_C = 354$ K, $\Delta T = 70$ K; $\Delta s \times E_0 = 0.039$, $\tau_0 = 7 \times 10^{-4}$ s. The red line is calculated at 1 Hz. The dashed line is the background E^0 .

consequent additional strain. In the FE case, the softening is of piezoelectric origin [51].

In view of the marked dependence on frequency shown in Fig. 3, the time dependence of the response of P to stress should be taken into account. This is usually done in the framework of the Landau-Khalatnikov theory, assuming that $\dot{P} = -(P - P_0)/(\chi L)$, where L is a nearly temperature independent kinetic coefficient and χ the susceptibility $\sim |T - T_C|^{-1}$, yielding a relaxation time $\tau = \tau_0/(T_C - T)$. Introducing this time dependence of P into the elastic response to a periodic excitation with angular frequency ω yields a complex compliance $\Delta S/(1 + i\omega\tau)$ [36, 52] and therefore a frequency dependence of the real part

$$\begin{aligned} \Delta S(\omega) &= \Delta S / [1 + (\omega\tau)^2] \\ \tau &= \tau_0 / (T_C - T) \end{aligned} \quad (5)$$

In order to fit the anomaly of the Young's modulus E with an expression like Eqs. (4–5), it is necessary to establish the background variation of $E(T)$. This usually is a linear stiffening during cooling, due to anharmonic effects, with quantum saturation below some temperature Θ , and can be written in terms of the compliance as [53]

$$1/E^0 = S^0 = S_0 + S_1 / \tanh(\Theta/T). \quad (6)$$

However, additional phenomena affect $E(T)$, as apparent in Figs. 1 and 2, and therefore a fit cannot be extended above 500 K, where a smooth frequency dependent kink is evident in Fig. 1. The low frequency experiment, spanning two decades in f , actually shows dependence of the background E^0 down to room temperature and is also noisier than in the resonance experiments. For this reason, we present a fit of the elastic anomaly measured during the 3rd cooling run in resonance,

when the sample had not yet been subjected to the various treatments with water. The best fit with Eqs. (4–6) is found with the parameters indicated in the caption to Fig. 4 (blue line). The red line is calculated at 1 Hz, in order to show the effect of the relaxation of the order parameter: increasing frequency, the minimum shifts to temperatures lower than T_C and its magnitude decreases. This is of the same type as observed in Fig. 3, though its full magnitude cannot be reproduced with Eq. (5). It is possible that a contribution to softening below the transition is also given by the motion of domain walls, which is typically larger at lower frequency [36], and may well explain the larger magnitude of the step at lower frequency.

As anticipated, Eq. (4) does not contain the contribution of fluctuations above T_C , and therefore cannot reproduce the evident precursor softening. Precursor softening is found commonly and in the classical ferroelectric BaTiO_3 it extends even to hundreds of kelvin above T_C [45]. It is notable that the Curie temperatures reported up to now for sliding ferroelectrics, WSe_2 [48] and WTe_2 [11, 15], are $T_C \simeq 350$ K as in our case.

These measurements demonstrate that nanoscale phenomena like FE in mono and bi-layers of vdW solids, generally studied with advanced techniques at the nanoscale, can be probed with mechanical spectroscopy on thick films. Notice that it is not necessary that the direction of the interlayer polarization is coherent along different pairs of layers, since strain is coupled to P^2 and strains from opposite polarizations do not cancel with each other.

The dissipation $Q^{-1}(T)$ of $\text{Ti}_3\text{C}_2\text{T}_x$ presents a positive step below T_C , which is the normal behaviour from the interaction between stress and the walls between the domains formed in the low-temperature phase [34, 36, 43]. With increase of temperature, the dissipation is dominated by intense relaxation processes with a broad spectrum of characteristic times toward high temperature (P2 in Fig. 1). Among the possible contributions to these losses are relative sliding of the flakes, hopping of the residual intercalated species, diffusion of the terminating molecules, and motion of point and extended defects within the monolayers.

The magnitude of the Young's modulus of the film consolidated in high vacuum at 970 K, $E = 40 - 50$ GPa, is larger than that achieved in $\text{Ti}_3\text{C}_2\text{T}_x$ densified by addition of sodium carboxymethyl cellulose and sodium borate (28 GPa) [54] or carboxymethylated cellulose nanofibrils (42 GPa) [55], but the films are fragile and E is still one order of magnitude smaller than the 330 GPa found with AFM on single flakes [56]. The large discrepancy between the in-plane Young's modulus of single and aggregated flakes must be due to their easy relative sliding.

We measured for the first time the temperature dependence of the complex Young's modulus E of the $\text{Ti}_3\text{C}_2\text{T}_x$ MXene in the form of self-standing thick films. In the as-prepared state the films have a very low $E \sim 4 - 10$ GPa, that may be increased up to 40 – 50 GPa by annealing in high vacuum at 970 K, so reducing the amount of intercalated species. This is still lower than 330 GPa of a single flake, presumably due to an easy relative sliding of the flakes, but allows reproducible anelastic spectra to be measured up to 900 K. The major fea-

ture is a phase transition below $T_C \sim 350$ K, producing a step-like softening of $\sim 4\%$ of E and increase of dissipation, which is robust against thermal treatments up to 900 K in vacuum or inert gas. The nature of the phase transition is discussed and it is concluded that it should be ferroelectric, based on the fact that the available structural and magnetic measurements exclude deviations from the hexagonal structure and magnetism at room temperature. Particular attention has been devoted to the mechanism of sliding ferroelectricity, where sliding of the layers with respect to each other induces charge transfer

between atoms/molecules belonging to the facing layers and hence to interlayer polarization. Notably, $T_C \simeq 350$ K is the same of other two known sliding ferroelectrics, WSe_2 has [48] and WTe_2 [11, 15]. This would add a new feature and perspectives of applications to the already numerous ones of $\text{Ti}_3\text{C}_2\text{T}_x$ MXene. In this view, the simple fact that this transition is slightly above room temperature calls for further investigations of its nature.

FC and ADC acknowledge the precious technical assistance of M.P. Latino (CNR-ISM).

-
- [1] Sung Hyuk Park, Jae Young Kim, Jae Yong Song, and Ho Won Jang. Overcoming Size Effects in Ferroelectric Thin Films. *Adv. Phys. Res.*, 2:2200096, 2023.
- [2] Ruixiang Fei, Wei Kang, and Li Yang. Ferroelectricity and Phase Transitions in Monolayer Group-IV Monochalcogenides. *Phys. Rev. Lett.*, 117:097601, 2016.
- [3] A. Belianinov, Q. He, A. Dziazgys, P. Maksymovych, E. Eliseev, A. Borisevich, A. Morozovska, J. Banys, Y. Vysochanskii, and S. V. Kalinin. CuInP_2S_6 Room Temperature Layered Ferroelectric. *Nano Lett.*, 15:3808, 2015.
- [4] Fucai Liu, Lu You, Kyle L. Seyler, Xiaobao Li, Peng Yu, Junhao Lin, Xuewen Wang, Jiadong Zhou, Hong Wang, Haiyong He, Sokrates T. Pantelides, Wu Zhou, Pradeep Sharma, Xiaodong Xu, Pulickel M. Ajayan, Junling Wang, and Zheng Liu. Room-temperature ferroelectricity in CuInP_2S_6 ultrathin flakes. *Nat. Commun.*, 7:12357, 2016.
- [5] Siyuan Wan, Yue Li, Wei Li, Xiaoyu Mao, Wenguang Zhu, and Hualing Zeng. Room-temperature ferroelectricity and a switchable diode effect in two-dimensional α - In_2Se_3 thin layers. *Nanoscale*, 10:14885, 2018.
- [6] Fengrui Sui, Min Jin, Yuanyuan Zhang, Ruijuan Qi, Yu-Ning Wu, Rong Huang, Fangyu Yue, and Junhao Chu. Sliding ferroelectricity in van der Waals layered γ - InSe semiconductor. *Nat. Commun.*, page 36, 2023.
- [7] Naoki Higashitarumizu, Hayami Kawamoto, Chien-Ju Lee, Bohan Lin, Fu-Hsien Chu, Itsuki Yonemori, Tomonori Nishimura, Katsunori Wakabayashi, Wen-Hao Chang, and Kosuke Nagashio. Purely in-plane ferroelectricity in monolayer SnS at room temperature. *Nat. Commun.*, 11:2428, 2020.
- [8] Kai Chang, Junwei Liu, Haicheng Lin, Na Wang, Kun Zhao, Anmin Zhang, Feng Jin, Yong Zhong, Xiaopeng Hu, Wenhui Duan, Qingming Zhang, Liang Fu, Qi-Kun Xue, Xi Chen, and Shuai-Hua Ji. Discovery of robust in-plane ferroelectricity in atomic-thick SnTe . *Science*, 353:274, 2016.
- [9] Shuoguo Yuan, Xin Luo, Hung Lit Chan, Chengcheng Xiao, Yawei Dai, Maohai Xie, and Jianhua Hao. Room-temperature ferroelectricity in MoTe_2 down to the atomic monolayer limit. *Nat. Commun.*, 10:1775, 2019.
- [10] A. Lipatov, P. Chaudhary, Z. Guan, H. Lu, G. Li, O. Crégut, K. D. Dorkenoo, R. Proksch, S. Cherifi-Hertel, D. F. Shao, E. Y. Tsymbal, J. Íñiguez, A. Sinitkii, and A. Gruverman. Direct observation of ferroelectricity in two-dimensional MoS_2 . *npj 2D Mater. Appl.*, 6:18, 2022.
- [11] Z. Fei, W. Zhao, T. A. Palomaki, B. Sun, M. K. Miller, Z. Zhao, J. Yan, X. Xu, and D. H. Cobden. Ferroelectric switching of a two-dimensional metal. *Nature*, 560:336, 2018.
- [12] Pankaj Sharma, Fei-Xiang Xiang, Ding-Fu Shao, Dawei Zhang, Evgeny Y. Tsymbal, Alex R. Hamilton, and Jan Seidel and. A room-temperature ferroelectric semimetal. *Sci. Adv.*, 5:eaax5080, 2019.
- [13] M. Vizner Stern, Y. Waschitz, W. Cao, I. Nevo, K. Watanabe, T. Taniguchi, E. Sela, M. Urbakh, O. Hod, and M. Ben Shalom. Interfacial ferroelectricity by van der Waals sliding. *Science*, 372:1462, 2021.
- [14] Astrid Weston, Eli G. Castanon, Vladimir Enaldiev, Fábio Ferreira, Shubhadeep Bhattacharjee, Shuigang Xu, Héctor Cortes-León, Zefei Wu, Nicholas Clark, Alex Summerfield, Teruo Hashimoto, Yunze Gao, Wendong Wang, Matthew Hamer, Harriet Read, Laura Fumagalli, Andrey V. Kretinin, Sarah J. Haigh, Olga Kazakova, A. K. Geim, Vladimir I. Falko, and Roman Gorbachev. Interfacial ferroelectricity in marginally twisted 2D semiconductors. *Nat. Nanotechnol.*, 17:390, 2022.
- [15] Qing Yang, Menghao Wu, and Ju Li. Origin of Two-Dimensional Vertical Ferroelectricity in WTe_2 Bilayer and Multilayer. *J. Phys. Chem. Lett.*, 9:7160, 2018.
- [16] Menghao Wu and Ju Li. Sliding ferroelectricity in 2D van der Waals materials: Related physics and future opportunities. *PNAS*, 118:e2115703118, 2021.
- [17] Shuhui Li, Feng Wang, Yanrong Wang, Jia Yang, Xinyuan Wang, Xueming Zhan, Jun He, and Zhenxing Wang. Van der Waals Ferroelectrics: Theories, Materials and Device Applications. *Advan. Mater.*, page 2301472, 2023.
- [18] Zhe Wang, Zhigang Gui, and Li Huang. Sliding ferroelectricity in bilayer honeycomb structures: A first-principles study. *Phys. Rev. B*, 107:035426, 2023.
- [19] Liu Yang, Shiping Ding, Jinhua Gao, and Menghao Wu. Atypical Sliding and Moiré Ferroelectricity in Pure Multilayer Graphene. *Phys. Rev. Lett.*, 131:096801, 2023.
- [20] Lei Li and Menghao Wu. Binary Compound Bilayer and Multilayer with Vertical Polarizations: Two-Dimensional Ferroelectrics, Multiferroics, and Nanogenerators. *ACS Nano*, 11:6382, 2017.
- [21] Jacob Parker and Yi Gu. van der Waals ferroelectrics: Progress and an outlook for future research directions. *J. Appl. Phys.*, 132:160901, 2022.
- [22] Anha Bhat, Shoaib Anwer, Kiesar Sideeq Bhat, M. Infas H. Mohideen, Kin Liao, and Ahsanulhaq Qurashi. Prospects challenges and stability of 2D MXenes for clean energy conversion and storage applications. *npj 2D Mater. Appl.*, 5:61, 2021.
- [23] Guohao Li, Shuhan Lian, Jie Wang, Guanshun Xie, Nan Zhang, and Xiuqiang Xie. Surface chemistry engineering and the applications of MXenes. *J. Materiomics*, 2023.
- [24] A. Agresti, A. Pazniak, S. Pescetelli, A. Di Vito, D. Rossi, A. Pecchia, M. Auf der Maur, A. Liedl, R. Larciprete, Denis V. Kuznetsov, D. Saranin, and A. Di Carlo. Titanium-carbide MXenes for work function and interface engineering in perovskite solar cells. *Nat. Mater.*, 18:1228, 2019.
- [25] Kanit Hantanasirisakul and Yuri Gogotsi. Electronic and Op-

- tical Properties of 2D Transition Metal Carbides and Nitrides (MXenes). *Adv. Mater.*, 30:1804779, 2018.
- [26] Yizhou Wang, Tianchao Guo, Zhengnan Tian, Lin Shi, Sharat C. Barman, and Husam N. Alshareef. MXenes for soft robotics. *Matter*, 6:2807, 2023.
- [27] Anand Chandrasekaran, Avani Mishra, and Abhishek Kumar Singh. Ferroelectricity, Antiferroelectricity, and Ultrathin 2D Electron/Hole Gas in Multifunctional Monolayer MXene. *Nano Lett.*, 4:3290, 2017.
- [28] Dongchen Tan, Chengming Jiang, Nan Sun, Jijie Huang, Zhe Zhang, Qingxiao Zhang, Jingyuan Bu, Sheng Bi, Qinglei Guo, and Jinhui Song. Piezoelectricity in monolayer MXene for nanogenerators and piezotronics. *Nano Energy*, 90:106528, 2021.
- [29] Dongchen Tan, Nan Sun, Long Chen, Jingyuan Bu, and Chengming Jiang. Piezoelectricity in Monolayer and Multilayer $Ti_3C_2T_x$ MXenes: Implications for Piezoelectric Devices. *ACS Appl. Nano Mater.*, 5:1034, 2022.
- [30] A. Lipatov, M. Alhabeab, M. R. Lukatskaya, A. Bosen, Y. Gogotsi, and A. Sinitiskii. Effect of Synthesis on Quality, Electronic Properties and Environmental Stability of Individual Monolayer Ti_3C_2 MXene Flakes. *Adv. Electron. Mater.*, 2:1600255, 2016.
- [31] F. Cordero, L. Dalla Bella, F. Corvasce, P. M. Latino, and A. Morbidini. An insert for anelastic spectroscopy measurements from 80 K to 1100 K. *Meas. Sci. Technol.*, 20:015702, 2009.
- [32] A. S. Nowick and B. S. Berry. *Anelastic Relaxation in Crystalline Solids*. Academic Press, New York, 1972.
- [33] W. Rehwald. The Study of Structural Phase Transitions by Means of Ultrasonic Experiments. *Adv. Phys.*, 22:721, 1973.
- [34] M. A. Carpenter and E. H. K. Salje. Elastic anomalies in minerals due to structural phase transitions. *Eur. J. Mineral.*, 10:693–812, 1998.
- [35] W. Schranz, H. Kabelka, and A. Tröster. Superelastic softening of ferroelastic multidomain crystals. *Ferroelectrics*, 426:242, 2012.
- [36] A. V. Kityk, W. Schranz, P. Sonderegeld, D. Havlik, E. K. H. Salje, and J. F. Scott. Low-frequency superelasticity and nonlinear elastic behavior of $SrTiO_3$ crystals. *Phys. Rev. B*, 61:946, 2000.
- [37] Haolin Jin, Kai Wang, Zhongquan Mao, Lingyun Tang, Jiang Zhang, and Xi Chen. The structural, magnetic, Raman and electrical transport properties of Mn intercalated $Ti_3C_2T_x$. *J. Phys.: Condens. Matter*, 34:015701, 2022.
- [38] Dipayan Sen, Gour Jana, Nitin Kaushal, Anamitra Mukherjee, and Tanusri Saha-Dasgupta. Intrinsic ferromagnetism in atomically thin two-dimensional organic-inorganic van der Waals crystals. *Phys. Rev. B*, 102:054411, 2020.
- [39] J. A. McNulty and P. Lightfoot. Structural chemistry of layered lead halide perovskites containing single octahedral layers. *IUCrJ*, 8:485, 2021.
- [40] A. M. Glazer. The classification of tilted octahedra in perovskites. *Acta Cryst. B*, 28:3384, 1972.
- [41] Tao Hu, Zhaojin Li, Minmin Hu, Jiemin Wang, Qingmiao Hu, Qingzhong Li, and Xiaohui Wang. Chemical Origin of Termination-Functionalized MXenes: $Ti_3C_2T_2$ as a Case Study. *J. Phys. Chem. C*, 121:19254, 2017.
- [42] Chenyang Shi, Majid Beidaghi, Michael Naguib, Olha Mashatalir, Yury Gogotsi, and Simon J. L. Billinge. Structure of Nanocrystalline Ti_3C_2 MXene Using Atomic Pair Distribution Function. *Phys. Rev. Lett.*, 112:125501, 2014.
- [43] F. Cordero. Quantitative evaluation of the piezoelectric response of unpoled ferroelectric ceramics from elastic and dielectric measurements: Tetragonal $BaTiO_3$. *J. Appl. Phys.*, 123:094103, 2018.
- [44] F. Cordero, F. Trequattrini, F. Craciun, H. T. Langhammer, D. A. B. Quiroga, and Jr. P. S. Silva. Probing ferroelectricity in highly conducting materials through their elastic response: Persistence of ferroelectricity in metallic $BaTiO_{3-d}$. *Phys. Rev. B*, 99:064106, 2019.
- [45] Francesco Cordero, Francesco Trequattrini, Paulo Sergio da Silva, Jr., Michel Venet, Oktay Aktas, and Ekhard K. H. Salje. Elastic precursor effects during $Ba_{1-x}Sr_xTiO_3$ ferroelastic phase transitions. *Phys. Rev. Research*, 5:013121, 2023.
- [46] Jun Xiao, Hanyu Zhu, Ying Wang, Wei Feng, Yunxia Hu, Arvind Dasgupta, Yimo Han, Yuan Wang, David A. Muller, Lane W. Martin, PingAn Hu, and Xiang Zhang. Intrinsic Two-Dimensional Ferroelectricity with Dipole Locking. *Phys. Rev. Lett.*, 120:227601, 2018.
- [47] Ping Tang and Gerrit E.W. Bauer. Sliding Phase Transition in Ferroelectric van der Waals Bilayers. *Phys. Rev. Lett.*, 130:176801, 2023.
- [48] Yang Liu, Song Liu, Baichang Li, Won Jong Yoo, and James Hone. Identifying the Transition Order in an Artificial Ferroelectric van der Waals Heterostructure. *Nano Lett.*, 22:1265, 2022.
- [49] M. E. Lines and A. M. Glass. *Principles and Applications of Ferroelectrics and Related Materials*. Oxford University Press, Oxford, 1977.
- [50] B. A. Strukov and A. P. Levanyuk. *Ferroelectric Phenomena in Crystals*. Springer, Heidelberg, 1998.
- [51] F. Cordero, F. Craciun, F. Trequattrini, and C. Galassi. Piezoelectric softening in ferroelectrics: ferroelectric versus antiferroelectric $PbZr_{1-x}Ti_xO_3$. *Phys. Rev. B*, 93:174111, 2016.
- [52] R. M. Yevych, Yu. M. Vysochanskii, M. M. Khoma, and S. I. Perechinskii. Lattice instability at phase transitions near the Lifshitz point in proper monoclinic ferroelectrics. *J. Phys.: Condens. Matter*, 18:4047–4064, 2006.
- [53] E.K.H. Salje, B. Wruck, and H. Thomas. Order-parameter saturation and low-temperature extension of Landau theory. *Z. Phys. B - Condensed Matter*, 82:399, 1991.
- [54] Sijie Wan, Xiang Li, Ying Chen, Nana Liu, Yi Du, Shixue Dou, Lei Jiang, and Qunfeng Cheng. High-strength scalable MXene films through bridging-induced densification. *Science*, 374:96, 2021.
- [55] Weiqian Tian, Armin VahidMohammadi, Michael S. Reid, Zhen Wang, Liangqi Ouyang, Johan Erlandsson, Torbjörn Pettersson, Lars Wågberg, Majid Beidaghi, and Mahiar M. Hamed. Multifunctional Nanocomposites with High Strength and Capacitance Using 2D MXene and 1D Nanocellulose. *Adv. Mater.*, 31:1902877, 2019.
- [56] A. Lipatov, H. Lu, M. Alhabeab, B. Anasori, A. Gruverman, Y. Gogotsi, and A. Sinitiskii. Elastic properties of 2D $Ti_3C_2T_x$ MXene monolayers and bilayers. *Sci. Adv.*, 4:eaat0491, 2018.

Supplemental Material to "Phase transition at 350 K in the $\text{Ti}_3\text{C}_2\text{T}_x$ MXene: possible sliding (moiré) ferroelectricity"

Francesco Cordero, Hanna Pazniak, Thierry Ouisse, Jesus Gonzalez-Julian, Aldo Di Carlo, Viktor Soprunyuk, Wilfried Schranz

I. ANELASTIC MEASUREMENTS - FREE FLEXURAL RESONANCE

The complex Young's modulus $E = E' + iE''$ was measured in an apparatus where a bar-shaped sample is suspended on thin thermocouple wires with a diameter of $50 \mu\text{m}$ in high vacuum ($< 10^{-5}$ mbar), and electrostatically excited on its free flexural resonant modes. The vibration is detected inserting the exciting electrode in a resonant circuit at ~ 13 MHz, whose frequency is modulated by the change of the capacitance between sample and electrode, and then demodulated to provide a signal proportional to the sample vibration [S1]. The resonance frequency of the fundamental flexural mode is [S2]

$$f = 1.028 \frac{h}{l^2} \sqrt{\frac{E}{\rho}}, \quad (\text{S1})$$

where l , h , ρ are the sample's length, thickness and density. The next four modes have frequencies in the ratios $1 : 2.8 : 5.49 : 9.07 : 13.5$, allowing the flexural modes to be distinguished from other types of vibrations. This is important with sample like these films, where the thickness is much less than the other dimensions and a large variety of modes can be excited. The variation of the sample dimensions due to the thermal expansion is usually negligible in comparison with respect to the change of the elastic moduli, so that the temperature dependence of E is evaluated as $E(T)/E_0 = [f(T)/f_0]^2$.

II. PRELIMINARY ANELASTIC MEASUREMENTS AND FLATTENING ANNEAL

The suspension thermocouple wires have a diameter of $50 \mu\text{m}$, and are in correspondence with the nodes of the 1st and 5th flexural modes, nearly coinciding, in order to minimize the coupling with the sample vibration. The sample must be fixed to the wires with drops of Ag paint at the edge, otherwise it would be attracted by the electrode. With samples as thin as the films studied here, having masses two orders of magnitude smaller than the typical samples used in the same apparatus, the intrinsic dissipation Q^{-1} is easily exceeded by extrinsic effects, such as the coupling with the wires, the Ag drops and the He exchange gas necessary to cool the sample below room temperature. At the lowest values of dissipation measured on these samples, $Q^{-1} < 10^{-3}$, exceeding 0.02 mbar of He already resulted in a clear increase of Q^{-1} . The $Q^{-1}(T)$ curves below room temperature have been corrected subtracting the step measured after the introduction of He. Also the resonance frequencies are affected by extrinsic effects, resulting in frequent jumps, whose amplitude is much larger for the vibration modes other than the 1st and 5th, for which the wires are not at the nodes of the vibration. After a number of measurements, we found a manner of coping with this problem, at least for the fundamental resonance, by applying a slight mechanical excitation to the sample holder before each measurement.

The first attempts to measure the complex Young's modulus of $\text{Ti}_3\text{C}_2\text{T}_x$ strips 10 to $80 \mu\text{m}$ thick and 12 to 28 mm long failed, because the strips bent considerably but reproducibly while heated or cooled in HV. In addition, there were too many resonances and it was difficult to single out those due to the flexural modes. Some of the resonances increased their frequency after heating beyond 700 K in HV, indicating near doubling of the elastic modulus after reaching 850 K. During this run, bubbles had developed on both faces with diameters of 1–2 mm, probably due to intercalated species that were prevented from being desorbed by a very small connected porosity.

The flexural resonance measurements reported here were made on a strip 25.5 mm long, 3 mm wide and $(73 \pm 4) \mu\text{m}$ thick, with the first three free flexural resonances clearly visible. In order to consolidate the film avoiding warping and bubbles, the sample was put between two alumina slabs 0.5 thick and heated at $1.5 \text{ }^\circ\text{C}/\text{min}$ up to $700 \text{ }^\circ\text{C}$ in 10^{-6} mbar, kept 1 h and furnace cooled. The film became flat and very brittle, and its Young's modulus increased from 11.9 GPa to 44 GPa. The consolidated sample could be measured exciting the 1st, 2nd, 3rd and 5th free flexural modes, whose frequencies ratios to the fundamental were within 6.7%, 4.7% and 1.1% of the theoretical values, respectively. The larger deviations were found in the 2nd and 3rd modes, for which the suspension wires did not match the nodes.

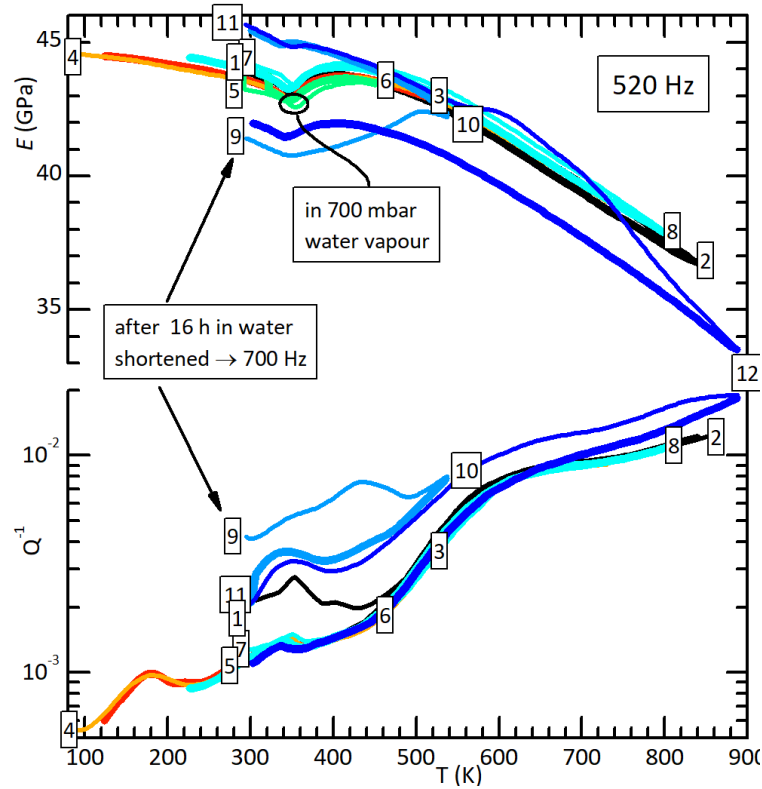


FIG. S1. Young's modulus and elastic energy loss measured during various heating (thin lines) and cooling (thick lines) runs exciting the 1st flexural mode. The numbers are placed at the start of the runs. After immersion in water, the sample was shortened and the resonance frequency passed from 520 to 702 Hz.

III. EFFECT OF WATER VAPOR AND IMMERSION IN WATER ON THE ANELASTIC SPECTRA

After the anelastic measurements of Fig. 1 two additional runs were conducted between room temperature and 890 and 410 K, in order to tune the experiment and verify that 14 h in air did not affect the anelastic spectrum. Afterwards the focus was to ascertain a possible influence of the terminations T_x and intercalated species on the phase transition. Figure S1 collects some of the salient temperature runs, including those in Figs. 1,2 (curves 2–4). The higher initial Q^{-1} of run 1 is attributed to the uncured fixing drops of Ag paint.

As a first attempt to intercalate H_2O , some drops of deionized water were put on the bottom of the quartz tube enclosing the insert, and the sample was measured in 700 mbar of air saturated with water vapor up to 450 K, maintained 1/2 h, and cooled to room temperature, for a total of 4 h in water vapor. Apart from a constant decrease of 1.5%, due to the effect of gas pressure on the vibration, the modulus presented exactly the same anomaly at T_C (curves 5, 6). The dissipation is not shown because it was large and featureless, due the damping effect of gas. Immediately after evacuating the humid air, modulus and dissipation were back at the original values, indicating that the intercalation of water had been absent or minimal. Repeating the measurements in HV produced the same curves as before exposure to humidity (curves 7, 8).

The next step was immersing the sample in deionized water for 2 h at 60 °C + 16 h at 22 °C with an intake $n \simeq 0.46$ of intercalated H_2O per formula unit, estimated from the mass increase. During 1.5 h in air the sample had lost ~ 0.053 H_2O per formula unit and an unknown amount in additional 2.5 h during which the sample was shortened due to difficulties in mounting. The amount of intercalated H_2O at the the start of run 9 was therefore $n \sim 0.32$ per formula unit. The effect (curve 9) is to increase the damping and soften the modulus and, from the recovery of both the $E(T)$ and $Q^{-1}(T)$ curves, it seems that the loss of intercalated H_2O is accelerated above 430 K in HV. The heating was limited to 536 K and curve 10 during cooling was higher than originally both in E and Q^{-1} , with a reduced step in E below T_C . During a final cycle up to 890 K in HV the original Q^{-1} curve was recovered, while E remained $\sim 4\%$ softer and the step amplitude was smaller than originally.

IV. DYNAMIC MECHANICAL ANALYZER

The anelastic spectra were measured also using a Perkin-Elmer Diamond DMA. Attempts at using the tension mode, where the sample is clamped at both ends, failed because clamping broke the samples. Therefore we used three point bending, where the sample is suspended on two metallic edges 5 mm apart and pushed in the centre by an edge-terminated rod. An alternate force is applied to the rod, in order to induce a vibration with an amplitude of up to 60 μm , corresponding to a maximum tensile strain of 7×10^{-4} , plus a constant force of 30 mN. All the measurements were performed in Ar atmosphere.

V. XRD, RAMAN, SEM

The structural properties of the free-standing films were studied by X-ray diffraction (XRD) and Raman spectroscopy. XRD patterns were recorded using a D8 Bruker diffractometer operating under the Bragg-Brentano geometry and equipped with Cu anode providing X-rays with 1.5406 Å wavelength. Raman measurements were performed in a backscattering configuration at room temperature, using an Ar⁺ laser radiation ($\lambda = 532$ nm), focused to a spot size around 0.8 μm on the sample surface. To avoid laser-induced sample degradation, we performed data acquisition at 0.5% laser power for 300 s. Raman spectra were calibrated by a silicon reference spectrum at room temperature.

To evaluate the quality of free-standing $\text{Ti}_3\text{C}_2\text{T}_x$ films and to follow possible changes after thermal annealing performed during anelastic measurements, we studied their structural properties, which are summarized in Fig. S2. As-prepared free-standing $\text{Ti}_3\text{C}_2\text{T}_x$ film consists of well delaminated flakes that are highly aligned along the c -direction, and only peaks from (00 l) planes are visible in the XRD pattern (Figure S2a).

The calculated c -lattice parameter of the as-prepared $\text{Ti}_3\text{C}_2\text{T}_x$ film corresponds to 26.35 Å. After the anneal at 700 °C and the anelastic measurements in high vacuum, we observed a shift in the peaks positions and a decrease in their intensity (Figure S2a). The shift in the peaks position is due to the loss of intercalants and, as a consequence, a decrease in the interplanar spacing between stacked MXene flakes. The c -lattice parameter of the $\text{Ti}_3\text{C}_2\text{T}_x$ film after the anelastic measurements is 20.22 Å, which is consistent with values reported for annealed $\text{Ti}_3\text{C}_2\text{T}_x$ MXenes [[S3]]. No new XRD peaks appeared after the anelastic measurements, excluding a change in the phase composition.

We then compare the Raman spectra of both films (Figure S2b). The Raman spectrum of the as-prepared film shows peaks previously observed for $\text{Ti}_3\text{C}_2\text{T}_x$ MXenes [[S4]]. The main A_{1g} mode, corresponding to out-of-plane vibrations of titanium atoms in the outer layer, carbon and surface groups, appears at 201 cm^{-1} . The second A_{1g} mode, corresponding to out-of-plane vibrations of carbon atoms, is located at 720 cm^{-1} . The broad peaks in the region of 230–470 cm^{-1} are attributed to in-plane vibrations of surface functional groups bonded with outer titanium atoms. The Raman spectrum measured on the film only subjected to DMA in Ar (data not shown) looks the same as the spectrum measured on as-prepared film. However, the sample from which the present results are obtained, produced a different spectrum. We observed the appearance of new peaks located at 149 cm^{-1} , 393 cm^{-1} , 516 cm^{-1} , and 635 cm^{-1} . These peaks correspond to the vibration modes of anatase. We note that the E_{1g} mode (149 cm^{-1}) of anatase has the highest intensity, while the intensity of the peaks belonging to the $\text{Ti}_3\text{C}_2\text{T}_x$ structure decreased significantly after the cycles of measurements. Due to the relatively shallow penetration depth of 532 nm light, we mainly probe 1 μm of the material. In this case, we attribute the formation of anatase to surface oxidation of $\text{Ti}_3\text{C}_2\text{T}_x$, since no TiO_2 peaks appear in XRD, probing the bulk of the film (Fig. S2a). We assume that surface oxidation occurred when the film was heated in air saturated with water.

VI. ELASTIC ANOMALY IN THE LANDAU THEORY

A derivation is presented of the elastic anomaly at a ferroelectric transition with spontaneous polarization P and a polarization p due to a temperature independent intrinsic piezoelectric effect of the non-centrosymmetric lattice under stress. The results in the absence of the piezoelectric polarization p are obtained setting $d = h = 0$.

Interlayer polarization of the sliding FE, mainly perpendicular to the layers: P

Intralayer piezoelectric polarization: p .

The Landau expansion of the Gibb's free energy $G = F - \sigma\varepsilon$ up to the 6th power of P is

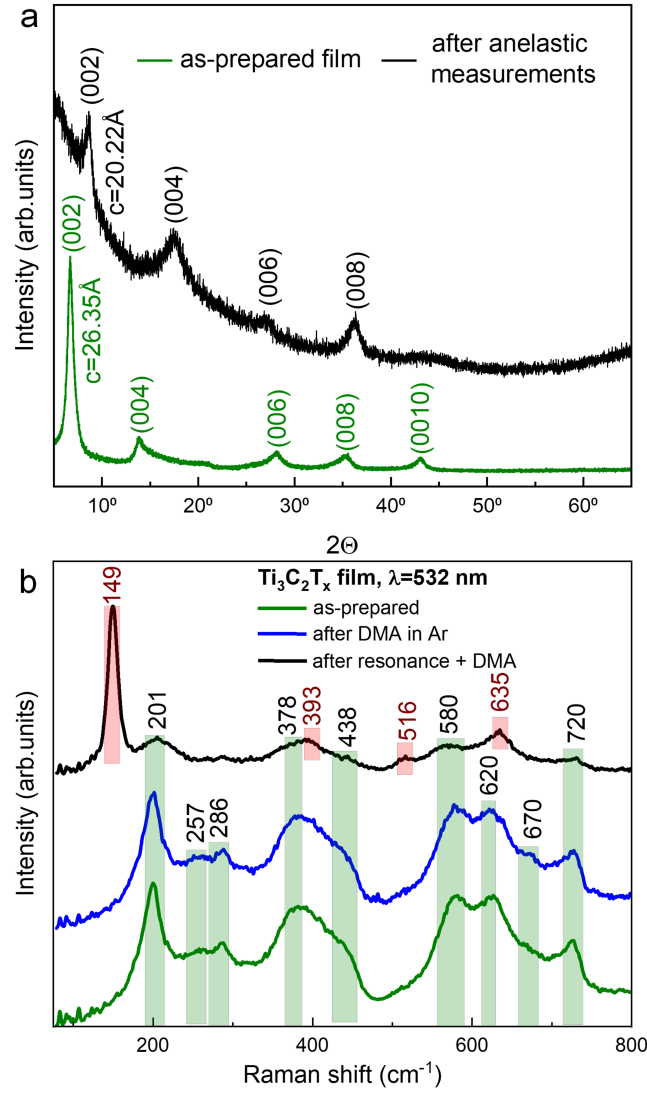


FIG. S2. XRD patterns (a) and Raman spectra (b) of as-prepared $\text{Ti}_3\text{C}_2\text{T}_x$ film and after the anelastic measurements. In the Raman spectra are marked the peaks corresponding to $\text{Ti}_3\text{C}_2\text{T}_x$ in green, and the peaks corresponding to TiO_2 (anatase phase) in pink.

$$\begin{aligned}
 G &= \frac{a(T - T_C)}{2} P^2 + \frac{B}{4} P^4 + \frac{C}{6} P^6 - \frac{S^0}{2} \sigma^2 - Q\sigma P^2 + \overbrace{\frac{1}{2\chi_p} p^2 - d\sigma p}^{G_p} \\
 &= \frac{1}{2} \underbrace{[a(T - T_C) - 2Q\sigma]}_{A'} P^2 + \frac{B}{4} P^4 + \frac{C}{6} P^6 - \frac{S^0}{2} \sigma^2 + G_p
 \end{aligned}$$

Find the equilibrium value p_0 of p in terms of the other variables, in order to eliminate it from G .

$$\begin{aligned}
 0 &= \frac{\partial G}{\partial p} = p/\chi_p - d\sigma \\
 p_0 &= \chi_p d\sigma
 \end{aligned}$$

Substituting into the Gibb's free energy

$$G_{p0} = G_p(P, p_0, \sigma) = -\frac{\chi_p}{2} (d\sigma)^2 \quad (\text{S2})$$

The spontaneous polarization P_0 in the stress-free state is similarly found

$$0 = A_P = \frac{\partial G_0}{\partial P} = (a(T - T_C) - 2Q\sigma)P + BP^3 + CP^5 \quad (\text{S3})$$

$$0 = A_P(\sigma = 0) = P [a(T - T_C) + BP^2 + CP^4] \quad (\text{S4})$$

whose solution is

$$P_0^2 = \frac{B}{2C} \left(\pm \sqrt{1 + \frac{4C}{B^2} a(T_C - T)} - 1 \right) = \quad (\text{S5})$$

$$= \frac{B}{2C} \left(\pm \sqrt{1 + \frac{T_C - T}{\Delta T}} - 1 \right) \begin{array}{l} + \quad B > 0, T < T_C \\ - \quad B < 0, T < T_C + \Delta T \\ + \quad B < 0, T_C < T < T_C + \Delta T \end{array} \quad (\text{S6})$$

$$\Delta T = \frac{B^2}{4aC} \quad (\text{S7})$$

The sign must give $P_0^2 > 0$ at low T :

when $B > 0$ it is + with $\sqrt{> 1} \rightarrow T < T_C$; the FE transition occurs at T_C ;

when $B < 0$ it is - with $\sqrt{> 0} \rightarrow \frac{T_C - T}{\Delta T} > -1 \rightarrow T < T_C + \Delta T$;

when $B < 0$ it is + for $\sqrt{-1 < 0} \rightarrow T_C - T < 0 \rightarrow T > T_C$.

When $B < 0$ there is possible coexistence of phases between T_C and $T_C + \Delta T$.

The compliance is

$$S = \frac{d\varepsilon}{d\sigma} = \frac{d}{d\sigma} \left(-\frac{\partial G}{\partial \sigma} \right) = \frac{d}{d\sigma} (QP^2 + S^0\sigma + \chi_p d^2\sigma) = S^0 + \chi_p d^2 + 2QP \frac{dP}{d\sigma}$$

To find $\frac{\partial P_0}{\partial \sigma}$ differentiate $A_P(\sigma) = 0$ (Eq. (3.2), $P \equiv P_0$):

$$\begin{aligned} 0 = \frac{dA_P}{d\sigma} &= \frac{d}{d\sigma} \{ P [a(T - T_C) + BP^2 + CP^4 - 2Q\sigma] \} = \\ &= \frac{\partial P_0}{\partial \sigma} \left\{ \overbrace{[a(T - T_C) + BP^2 + CP^4]}^{=0 \text{ (Eq. 3.3)}} - \overbrace{2Q\sigma}^{=0 \text{ stress-free state}} \right\} + P \left[+2BP \frac{\partial P_0}{\partial \sigma} + 4CP^3 \frac{\partial P_0}{\partial \sigma} - 2Q \right] = \\ &= P \frac{\partial P_0}{\partial \sigma} [2BP + 4CP^3] - 2QP = 0 \\ \frac{\partial P_0}{\partial \sigma} &= \frac{2QP}{2BP^2 + 4CP^4} \end{aligned}$$

When $P = P_0 > 0$

$$\Delta S = S - S^0 = \chi_p d^2 + \frac{2Q^2}{B + 2CP_0^2} = \chi_p d^2 + \frac{2Q^2}{\|B\| \sqrt{1 + \frac{T_C - T}{\Delta T}}} \quad (\text{S8})$$

[S1] F. Cordero, L. Dalla Bella, F. Corvasce, P. M. Latino, and A. Morbidini, An insert for anelastic spectroscopy measurements from 80 K to 1100 K. *Meas. Sci. Technol.*, 20, 015702 (2009).

- [S2] A. S. Nowick and B. S. Berry, *Anelastic Relaxation in Crystalline Solids*. Academic Press, New York, 1972.
- [S3] N. C. Osti *et al.* Effect of Metal Ion Intercalation on the Structure of MXene and Water Dynamics on its Internal Surfaces. *ACS Appl. Mater. Interfaces*, 8, 8859 (2016).
- [S4] A. Sarycheva and Y. Gogotsi, Raman Spectroscopy Analysis of the Structure and Surface Chemistry of $\text{Ti}_3\text{C}_2\text{T}_x$ MXene. *Chem. Mater.*, 32, 3480 (2020).